PCCP
Physical Chemistry Chemical Physics

Accepted Manuscript

This article can be cited before page numbers have been issued, to do this please use: L. Tacconi and M. Perfetti, *Phys. Chem. Chem. Phys.*, 2026, DOI: 10.1039/D6CP00980H.

ROYAL SOCIETY OF CHEMISTRY

rsc.li/pccp

View Article Online
DOI: 10.1039/D6CP00980H

Easy axis crystal field limit in trivalent lanthanide complexes: expected magnetization, susceptibility, magnetic torque and XMCD signatures.

Leonardo Tacconi[†*] and Mauro Perfetti[†*]

[†] Department of Chemistry "Ugo Schiff" & INSTM RU, Università degli Studi di Firenze, Via della Lastruccia 3, 50019, Sesto F.no (FI), Italy

*leonardo.tacconi@unifi.it, *mauro.perfetti@unifi.it

Abstract

Lanthanide complexes exhibiting marked easy axis magnetic anisotropy are the main targets to achieve highly performant Single Molecule Magnets, Pseudo Contact Shift Agents and Rotating Magnetic Refrigerants. To experimentally map the magnetic anisotropy orientation and magnitude, a growing portfolio of experimental techniques is now available, including powder and single crystal magnetometry, cantilever torque magnetometry, and X-ray Magnetic Circular Dichroism. While these methods provide complementary information, reference values for ideal systems are not always applied consistently, possibly introducing ambiguity in data interpretation. Here we present a unified and quantitative set of benchmark magnetic observables for trivalent lanthanide ions exhibiting strong easy-axis anisotropy. For each ion we report: the orientation-dependent saturation magnetization and low-temperature magnetic susceptibility; the field-dependent maximum magnetic torque signal; and the angular- and field-dependent normalized XMCD response at the $M_{4,5}$ edges. The resulting tables and figures provide a simple, ready-to-use reference framework for direct comparison with experimental measurements of lanthanide-based magnetic systems.

Introduction

"The experimentally measured observable reaches the expected value" is a common statement in scientific literature. When supported by appropriate references, such agreement validates the reliability of a measurement and helps quantify deviations from ideal behavior. Comparison with expected values also provides qualitative insight into the

View Article Online
DOI: 10.1039/D5CP00980H

observed phenomena and offers simple, computationally inexpensive guidelines for optimizing the desired properties.

In molecular magnetism, this statement most frequently refers to the magnetic moment of a sample — the primary quantity measured in magnetometric studies.[1] Traditionally, most measurements are performed on powder samples because of their simplicity and rapid data acquisition.[2] However, in recent years powder magnetometry has increasingly been complemented or replaced by single crystal[3] and torque magnetometry[4]. In parallel, growing interest has emerged in probing magnetic molecules deposited on surfaces, typically via highly sensitive spectroscopic techniques such as X-ray Magnetic Circular Dichroism (XMCD)[5], largely motivated by potential applications in areas such as molecular memory storage[6] and spintronics[7].

While combining multiple experimental techniques provides complementary information, the reference values expected for ideal systems are not always applied consistently. As a result, the interpretation of experimental data can become ambiguous, particularly when comparing results obtained from powders, single crystals, torque measurements, or surface-sensitive spectroscopies. To our knowledge, no unified set of reference values encompassing the major experimental techniques has been established for lanthanide-based magnetic systems.

A target property to design and finely tune for achieving performant magnetic materials is the magnetic anisotropy, i.e. the spatial dependence of the magnetic response of the material. Among the anisotropy shapes that can be achieved, one is surely the most targeted: easy axis magnetic anisotropy. Such anisotropy implies that the molecule can be easily magnetized when a magnetic field is applied along a certain direction (the easy axis) while when the field is along the perpendicular plane the magnetic moment is negligible. Therefore, when chemically designed, lanthanide based molecular complexes are ideal for achieving highly performant Single Molecule Magnets, Pseudo Contact Shift Agents and Rotating Magnetic Coolants. A review on its role in boosting the properties of these materials has been recently published.[8]

Since easy axis magnetic anisotropy is a well-established target, in this contribution we present a series of tables and graphs summarizing the values of key observables expected for ideal easy-axis lanthanide systems. To provide a simple, ready-to-use and transparent reference framework, we analyze the limiting case of a perfectly axial system (i.e. no mixing between states). Although real systems often deviate from this idealized limit, it represents the best-case scenario for many applications of lanthanide molecular magnets, and it has been achieved in single-molecule magnets[9–11], pseudo-contact shift agents[12,13], and rotating

View Article Online
DOI: 10.1039/D0CP00980H

magnetocaloric materials[14,15]. The values reported here therefore provide a convenient benchmark to estimate the deviation of experimental results from ideal behaviour.

Experimental

Magnetometry. Magnetization, magnetic susceptibility and torque data were simulated using in-house MATLAB scripts based on the *EasySpin* package (v. 6.0.2).[16] DC magnetometry data were computed for both the *z* and *x* magnetic directions of an oriented single crystal, as well as for a powder ensemble. Torque magnetometry was simulated by considering the rotation of a single crystal about the *x* magnetic axis, with the magnetic field aligned along the principal *z* axis at zero rotation angle.

X-ray Magnetic Circular Dichroism. Polarization-dependent absorption and XMCD spectra were simulated using a custom script based on the script language *Quanty*.[17] Temperature effects were included by weighting transition probabilities according to the Boltzmann population of the initial states. A Lorentzian broadening was applied to account for finite state lifetimes.

Results and Discussion

Orbital Asphericity and Magnetic Anisotropy in Lanthanides

The magnetic properties of lanthanides originate from the unique characteristics of the 4f orbitals.[18] Unlike d orbitals, 4f orbitals are strongly shielded by the filled 5s and 5p shells, lying deep within the atomic core.[19] As a consequence, ligand-lanthanide interactions are largely ionic and the spin orbit interaction remains essentially unquenched. The electronic structure is therefore organized into well-separated (10^3-10^4 cm^{-1}) spin-orbit coupled *J* manifolds, which are further split by the Crystal Field (CF, of the order of 10^2-10^3 cm^{-1}). Therefore, CF-induced mixing between different *J* multiplets is typically negligible, and the magnetic properties at room temperature and below can usually be described by considering only the ground *J* manifold.[20]

Within this framework, the magnetic behaviour of lanthanide ions is determined by the energy of the $|J,m_J\rangle$ states in the CF potential generated by the surrounding ligands. In the simplest case, their ordering can be rationalized using an electrostatic model[21], in which the key quantity is the charge density asphericity of the $|J,m_J\rangle$ states — first derived by Sievers[22] and later popularized by Rinehart and Long[23]. In particular, the angular dependence of the charge density for a given $|J,m_J\rangle$ state can be expressed as

$$R(\theta) = \sqrt[3]{c_0 + c_2 Y_2^0(\theta) + c_4 Y_4^0(\theta) + c_6 Y_6^0(\theta)} \quad (1)$$

View Article Online
DOI: 10.1039/D6CP00980H

where Y_k^0 are the spherical harmonics and c_k are the multipole moments of rank k. These coefficients are given by

$$c_0 = \frac{n}{\sqrt{4\pi}}, \quad c_k = A_k \sqrt{\frac{2k+1}{4\pi}} \ (k = 2,4,6) \tag{2}$$

with n the number of 4f electrons. The factors A_k encode the angular anisotropy of the $|J,m_J\rangle$ wavefunction and are obtained by projecting the rank k spherical tensor C_k^0 onto the ground state J multiplet. Therefore, the resulting expressions depend explicitly on both J and m_J, and the corresponding coefficients for each lanthanide ion are tabulated in the literature.[22] Importantly, the charge densities are expressed in terms of spherical harmonics with $m = 0$, which exhibit cylindrical symmetry about the quantization axis, as they depend only on the polar angle θ and not on the azimuthal angle ϕ. In this case, a three-dimensional isosurface representation corresponds to a surface of revolution of $R(\theta)$ and does not provide additional information beyond the angular dependence clearly depicted in simple polar plots.

Since this work focuses on idealized benchmark systems, Figure 1 highlights the polar plots of the largest and smallest m_J states' electron density for each trivalent ion, corresponding to ideal easy-axis and easy-plane magnetic anisotropy, respectively. All $|J,m_J\rangle$ states are reported in Figure S1. In the representation shown in Figure 1 and Figure S1, an isotropic contribution was subtracted from all surfaces to emphasize the anisotropic component of the charge density. Therefore, the plotted quantity should be understood as a visualization of the deviation from spherical symmetry rather than as the full charge density. Each row of Figure 1 groups ions differing by seven 4f electrons, and thus sharing the same orbital angular momentum, highlighting the similarities in their electron densities.[24] This arrangement reveals the pronounced evolution of orbital asphericity across the lanthanide series and its strong dependence on m_J, spanning from prolate to oblate shapes. These differences reflect the multipolar character of the 4f shell and anticipate the strongly anisotropic magnetic response of different $|m_J|$ states.

In general, oblate charge distributions are preferentially stabilized by axial crystal fields, whereas prolate charge distributions are stabilized by equatorial ligand arrangements. This electrostatic picture provides an intuitive link between orbital asphericity, and the crystal field Hamiltonian used to describe the energy level structure.[21,23]

View Article Online
DOI: 10.1039/D6CP00980H

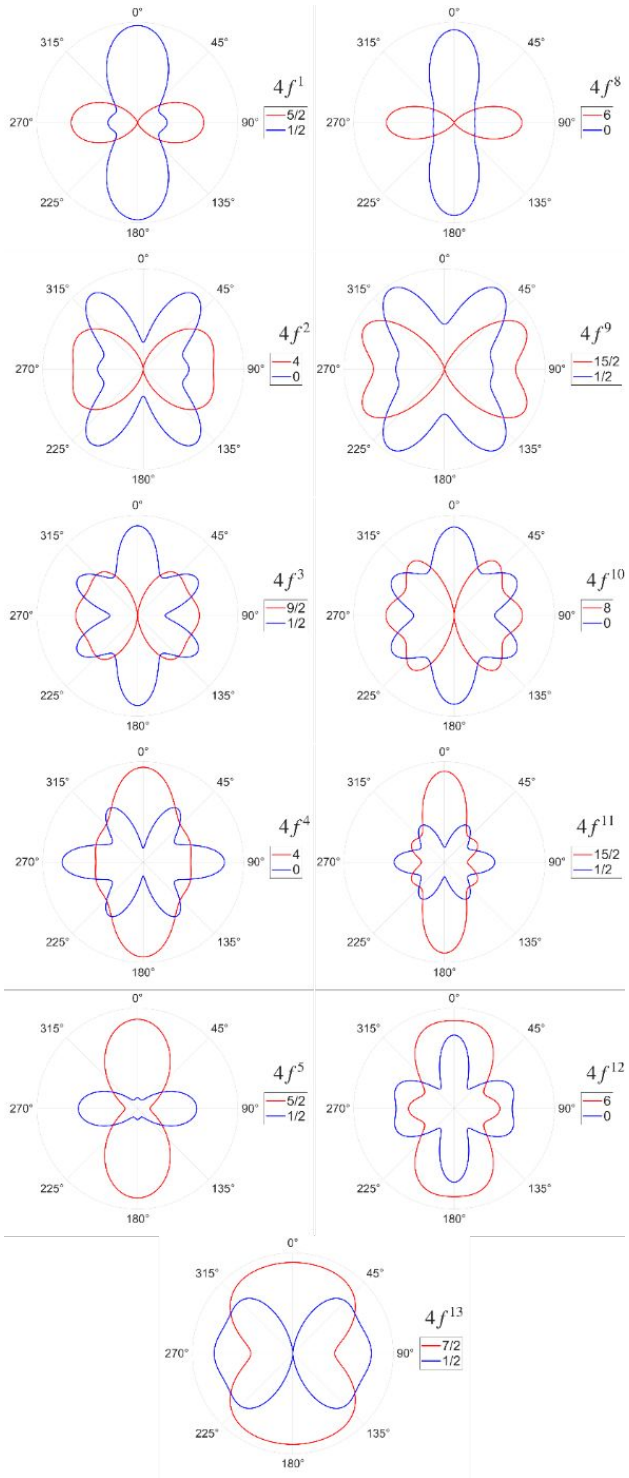

Figure 1 – Asphericity of the $|J,m_J\rangle$ (m_J = $\pm J$ and 0 or $\pm 1/2$ for non-Kramers and Kramers ions, respectively) components of Ln(III), calculated using equations reported by Sievers.[22] Each row of the Figure compares ions differing by 7 f-electrons. The red and blue trace always correspond to the maximum and minimum m_J, respectively.

The crystal field potential at the lanthanide centre is described by the CF Hamiltonian

$$H_{CF}(\hat{J}) = \sum_{k=2,4,6} \sum_{q=-k}^{k} B_k^q \hat{O}_k^q(J)\,. \qquad (3)$$

View Article Online
DOI: 10.1039/D6CP00980H

where B_k^q are the CF parameters and $\hat{O}_k^q(J)$ are the Stevens equivalent operators[25] projected onto the Russell-Saunders ground state J manifold.[26] In real complexes the full expansion can contain up to 27 parameters[27], and symmetry can lower this number significantly. These operators are polynomials of $\hat{J}_z$ and the ladder operators $\hat{J}_\pm$ and can be divided into diagonal and off-diagonal operators. Diagonal operators depend exclusively on powers of $\hat{J}_z$ and therefore do not mix the $|J,m_J\rangle$ states. A purely uniaxial anisotropy can thus be described by the second rank axial operator

$$\hat{O}_2^0 = 3\hat{J}_z^2 - J(J+1). \quad (4)$$

Under the sole action of this operator, the energy of each $|J,m_J\rangle$ state becomes

$$E\big(|J,m_J\rangle\big) \propto 3m_J^2 - J(J+1) \quad (5)$$

which depends quadratically on m_J, reaching its maximum for the largest $|m_J|$ and its minimum for the smallest $|m_J|$. The sign of B_2^0 therefore uniquely determines the level ordering and the resulting magnetic anisotropy. A negative B_2^0 stabilizes the largest $|m_J|$, yielding easy-axis anisotropy.

This transparent ordering mechanism naturally defines the axial anisotropy regime, which forms the basis of the model adopted throughout this work. For each ion, the magnitude of B_2^0 was adjusted such that the energy separation between the ground and first excited states is fixed at 300 cm^{-1}. Such a gap assures that at T = 2 K, at which we simulate all the benchmark values, only the pure $|\pm m_J\rangle$ ground state (with $|m_J| = J$) is populated while keeping the overall CF splitting below the spin-orbit interaction, thereby preserving the hierarchy of energy scales characteristic of trivalent lanthanides. Moreover, this relatively large energy gap strongly suppresses the contribution of excited states to the magnetic behaviour also in terms of the field-induced mixing via the Zeeman interaction. The CF parameters employed and the corresponding energy schemes are provided in Table S1. Although idealized, this model yields benchmark values that are consistent with those reported for strongly axial lanthanide complexes[28–30], supporting its use as a practical reference for assessing how closely real systems approach the easy-axis limit.

Importantly, among the thirteen trivalent lanthanide ions, we exclude from our analysis Eu(III) and Gd(III) due to their specific electronic structures. According to Hund's rules, Eu(III) has a singlet ground term ($J = 0$), arising from the cancellation of the $L = 3$ and $S = 3$ angular momenta. Consequently, its magnetic behaviour is weak and dominated by temperature-independent paramagnetism. In contrast, Gd(III) has 7 f-electrons, leading to $L = 0$. Therefore, its ground state presents negligible magnetic anisotropy. Since the present work focuses on the role of orbital anisotropy in determining magnetic behaviour, these two ions fall outside the scope of the analysis.

View Article Online
DOI: 10.1039/D6CP00980H

Benchmark Magnetic Observables

Molecular magnetic materials can be probed by a variety of experimental techniques, each providing complementary information on the electronic structure and magnetic anisotropy of the complexes under study. In this work we focus on four key magnetic observables that can be directly compared across the lanthanide series within the axial anisotropy framework described above: (i) the low-temperature, high-field magnetization; (ii) the low-temperature, low-field magnetic susceptibility (χT); (iii) the field-dependent maximum magnetic torque; and (iv) the angular dependent XMCD peak intensity at the $M_{4,5}$ edges. A schematic representation of the magnetic observables considered in this work is shown in Figure 2. All computational details are described in Methods.

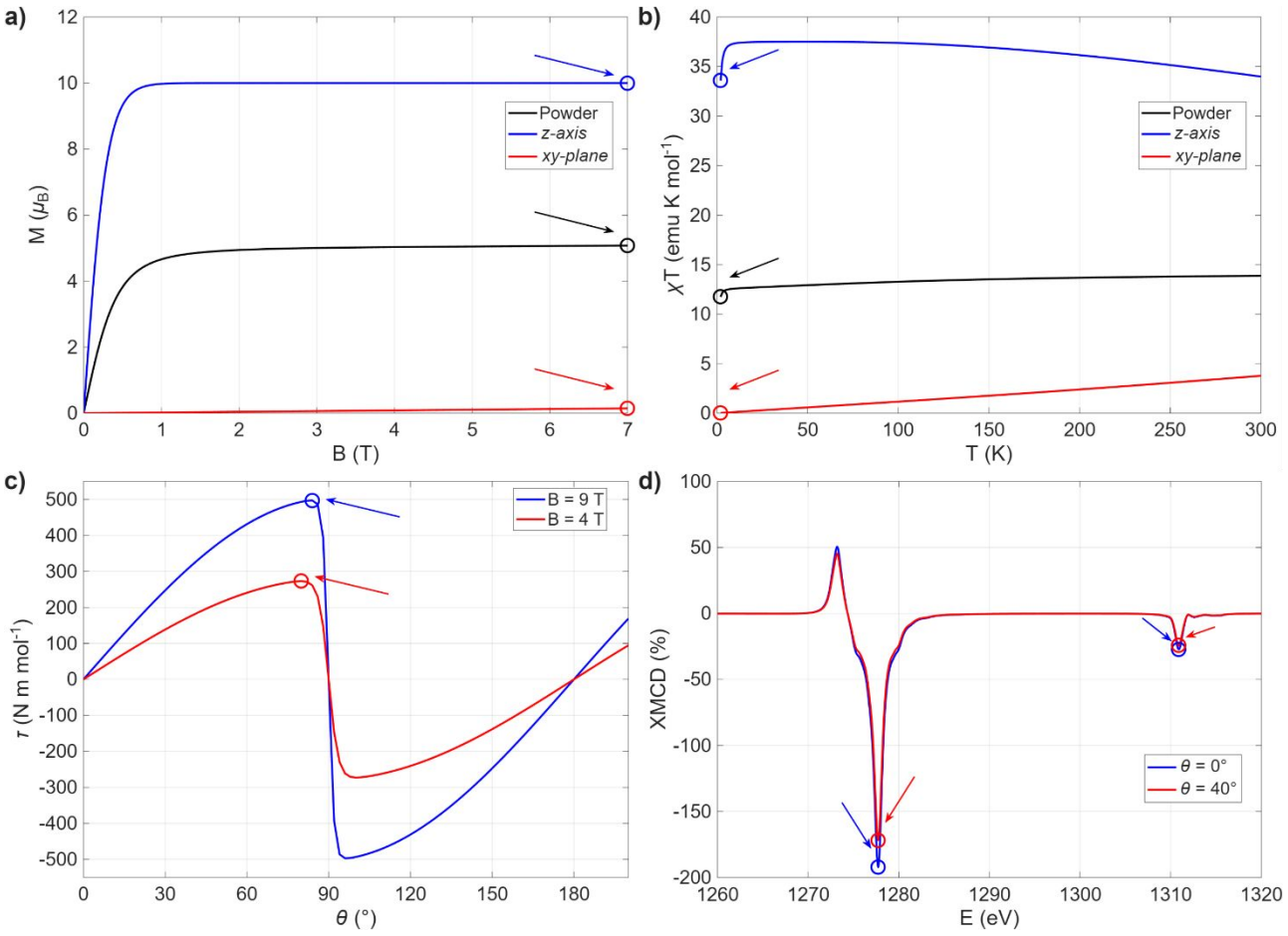

Figure 2 – Schematic representation of the magnetic observables of interest computed in this work for an exemplary Dy^{3+} ion: orientation-dependent low-temperature and high-field magnetization (**a**); orientation-dependent low-temperature and low-field magnetic susceptibility χT (**b**); field-dependent maximum magnetic torque (**c**); angular-dependent XMCD peak intensity at the $M_{4,5}$ edges (**d**).

Magnetization

DC magnetometry is one of the most widely used techniques for characterizing molecular magnetic complexes and can be applied to both powder samples[31,32] and oriented single crystals[33,34]. The magnetic response of a lanthanide ion in an external magnetic field is governed by the Zeeman interaction:

$$\hat{H}_{Zeeman} = \mu_B g_J \vec{B} \cdot \hat{J} = \mu_B g_J \left(B_x \hat{J}_x + B_y \hat{J}_y + B_z \hat{J}_z\right). \quad (6)$$

where g_J is the Landé factor and $\hat{J}$ is the total angular momentum operator. This expression is valid in the weak-field regime, where the spin-orbit coupling dominates over the Zeeman interaction and J remains a good quantum number. In this limit, the Zeeman Hamiltonian can be expressed in terms of $\hat{J}$ upon projection onto the $|J,m_J\rangle$ manifold.

The orientation of the magnetic field relative to the magnetic anisotropy axis plays a central role in determining the magnetic response. When the magnetic field is applied along the z magnetic axis, it couples to $\hat{J}_z$, which is diagonal in the $|J,m_J\rangle$ basis. In this configuration the magnetization is determined solely by the identity and thermal population of the crystal field levels. By contrast, a transverse magnetic field couples through $\hat{J}_x$ and $\hat{J}_y$, which contain the ladder operators $\hat{J}_\pm$ and therefore mix the ground state with excited states. The magnitude of this mixing is primarily governed by the energy separation between the ground and excited crystal field states. An example of the role of the energy gap on the magnetic response is provided in Figure S2, where magnetization curves at T=2 K for a Dy(III) ion are simulated for different energy separations. As shown in the figure, decreasing the energy gap leads to a progressive deviation from the ideal horizontal plateau at high fields, reflecting the increasing contribution of field-induced mixing with excited states, commonly associated with temperature-independent paramagnetism (TIP).

For these reasons, the orientation-dependent saturation magnetization provides a direct experimental probe of the axial character of the ground state. In this work the saturation magnetization was simulated at 2 K and 7 T, conditions readily accessible with commercial magnetometers. Three orientational configurations were considered: along the principal magnetic axis z, within the isotropic xy plane, and as an orientational average over a powder sample. The resulting values are reported in Figure 3.

View Article Online
DOI: 10.1039/D6CP00980H

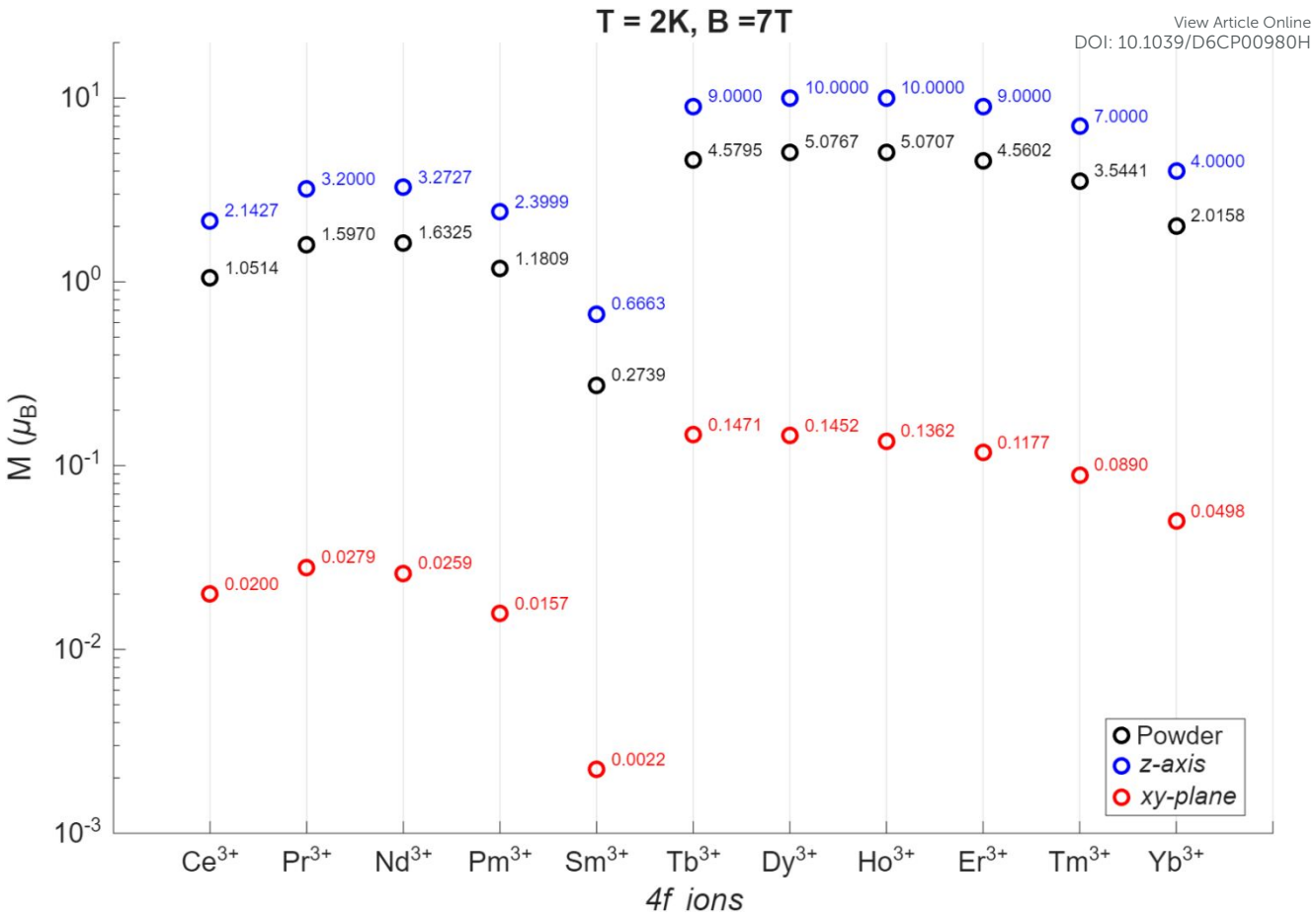

Figure 3 – Expected magnetization values calculated for lanthanide ions with an easy-axis magnetic anisotropy. Eu^{3+} and Gd^{3+} have not been included due to their $J = 0$ and $L = 0$ ground state, respectively.

As expected, the largest magnetization is obtained when the magnetic field is applied along the z axis. In this configuration the saturation is well described by

$$M_{sat} = g_J|m_J| \approx \left(1 + \frac{J(J+1) - L(L+1) + S(S+1)}{2J(J+1)}\right)|m_J| \qquad (7)$$

where $|m_J|$ corresponds to the ground state crystal field component. By contrast, the magnetization within the equatorial xy plane is strongly suppressed and approaches zero in the ideal limit. The small residual magnetization in this configuration arises from field-induced mixing between the ground and excited states and is therefore inversely proportional to the energy gap between these levels (fixed to 300 cm^{-1} at zero field in our model). At low temperature, the axial saturation value is reached at relatively small fields, whereas the transverse magnetization increases approximately linearly with field, reflecting the weak mixing induced by the transverse Zeeman term. This is illustrated for an ideal Dy(III) ion in Figure S3.

View Article Online
DOI: 10.1039/D6CP00980H

For powder samples the measured magnetization corresponds to an orientational average over all possible directions of the magnetic field relative to the molecular anisotropy axes. The powder magnetization is therefore given by

$$M_{powder} = \frac{1}{4\pi}\int_0^{2\pi}\int_0^{\pi} M(\theta,\varphi)\sin\theta\, d\theta d\varphi\,. \tag{8}$$

For uniaxial systems, where the xy plane is isotropic and the magnetization depends only on the polar angle θ, this equation simplifies to

$$M_{powder} = \frac{1}{2}\int_0^{\pi} M(\theta)\sin\theta\, d\theta\,. \tag{9}$$

In practice, this integral is evaluated numerically by computing the magnetization at a discrete set of orientations distributed uniformly over a sphere. Lebedev quadrature[35] provides an efficient spherical sampling scheme, yielding accurate powder averages with a relatively small number of orientations.[36,37] However, increasing the number of grid points raises computational cost, which can become significant for field- and temperature-dependent simulations. A commonly used simplified alternative is the so-called "thirds" approximation[38,39], in which the powder magnetization is approximated as the arithmetic mean of the principal components:

$$M_{thirds} = \frac{M_x + M_y + M_z}{3}. \tag{10}$$

Figure S4Figure 3 shows that this approximation can yield substantially different results from a rigorous spherical average in the low-temperature, high-field regime. This discrepancy is further illustrated in Figure S5, where the temperature- and field-dependent powder magnetization curves for an easy-axis Dy^{3+} centre are compared using both approaches. The "thirds" approximation systemically underestimates the powder magnetization, a direct consequence of the highly anisotropic magnetization tensor in the easy-axis regime. Its use in quantitative simulations of anisotropic powder samples should therefore be approached with caution.

It is worth noting that the powder saturation magnetization value alone is not a clear indication of the nature of the ground state doublet of the investigated sample. As a matter of fact, a powder saturation value of around 5 μ_B for a Dy^{3+} ion can also be obtained for ground states with significantly different compositions, as evidenced in Figure S6. This arises because powder magnetization measurements correspond to an orientational average over all possible directions of the applied magnetic field, which can shade the correct wavefunctions. In other words, different combinations of $|m_J|$ components may lead to

View Article Online
DOI: 10.1039/D5CP00980H

similar powder saturation values. For this reason, the saturation magnetization alone cannot be considered a definitive fingerprint of the ground state. What provides more reliable insight into the ground state composition is the field dependence of the magnetization, the comparison between single crystal magnetization values measured parallel and perpendicular to the principal magnetic axis, and the comparison with other experimental techniques.

Magnetic Susceptibility

Magnetic susceptibility measurements provide complementary information to field-dependent magnetization and are routinely obtained using DC magnetometry. In principle, the magnetic susceptibility tensor is rigorously defined as the field derivative of the magnetization.[40]

$$\chi = \frac{\partial M}{\partial H} \tag{11}$$

In experimental practice, however, susceptibility is commonly approximated by measuring the magnetic moment and dividing it by the applied field, yielding

$$\chi = \frac{M}{H} \tag{12}$$

These two expressions only coincide when the magnetization varies linearly with the applied magnetic field. This distinction is important, as deviations from linearity can lead to noticeable differences between simulated susceptibilities and experimentally reported values.

Magnetic susceptibility is most reported as the product χT as a function of temperature. At high temperatures, χT approaches the Curie constant expected for the free ion, which can be calculated directly from the quantum number J and g_J.

At low temperature and low magnetic field, however, the situation is markedly different. Under these conditions only the lowest CF level is significantly populated, and the magnetic response becomes dominated by the nature of the ground state. The resulting χT value therefore provides a hint regarding the ground state anisotropy. For this reason, calculations were performed under experimentally accessible conditions (T = 2 K, B = 0.1 T) for the three relevant configurations discussed above. The resulting values are summarized in Figure 4.

As observed for magnetization data, the calculated χT values clearly reflect the strongly anisotropic nature of the easy-axis ground state. The xy-plane susceptibilities remain close to zero across the entire lanthanide series, whereas the axial susceptibilities are significantly larger due to the strong magnetic moment associated with the ground state $|m_J|$ component.

View Article Online
DOI: 10.1039/D6CP00980H

The "thirds" approximation works well at these low field, especially for light ions (Figure S7). Nevertheless, a non-negligible discrepancy persists for late-series ions, where deviations up to approximately 5% are observed. These results highlight the intrinsic limitations of the approximation and further support the use of spherical averaging when quantitative simulations of anisotropic powder samples are required.

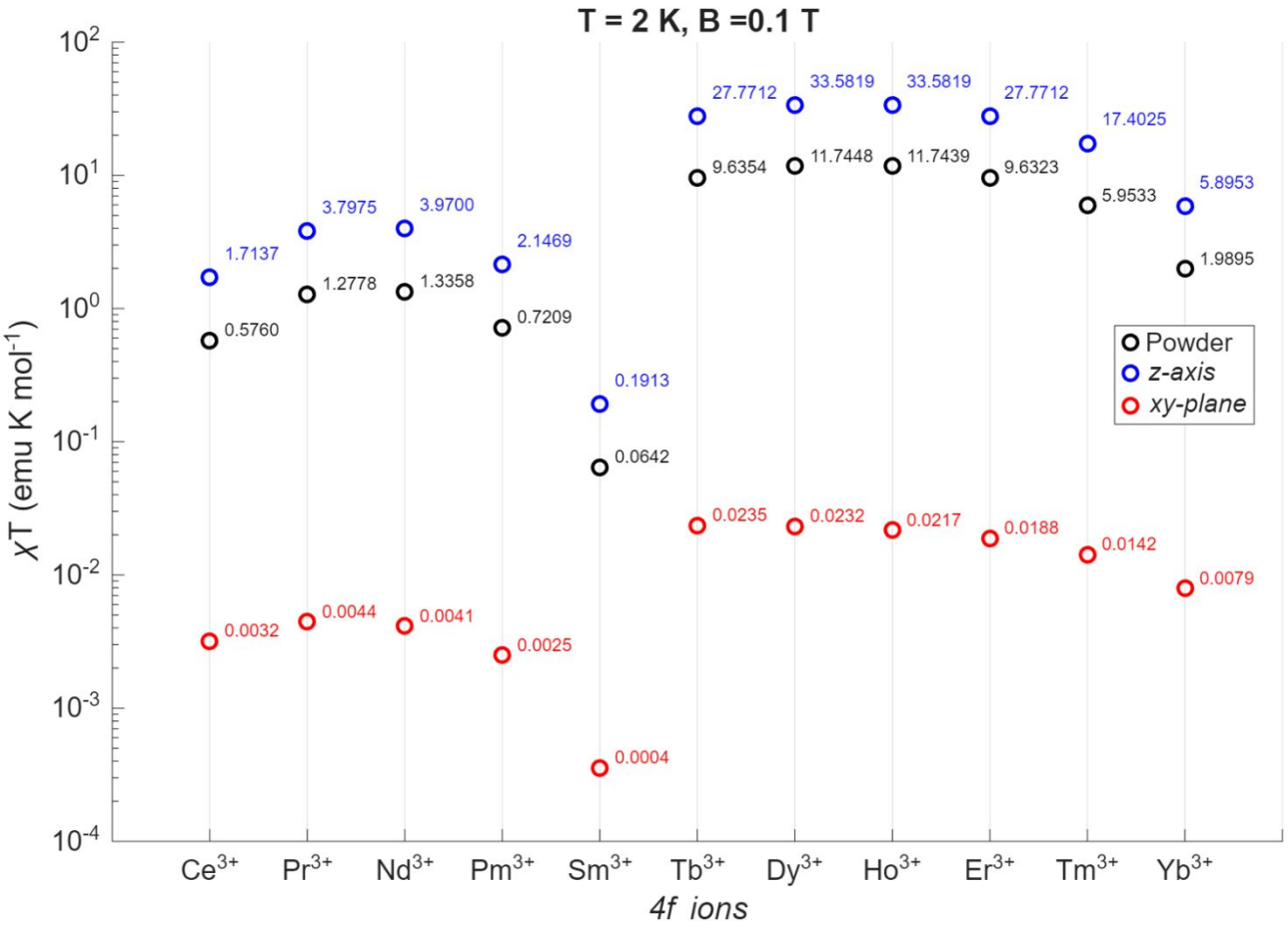

Figure 4 – Expected χT values calculated for lanthanide ions with an easy-axis magnetic anisotropy. Eu^{3+} and Gd^{3+} have not been included due to their $J = 0$ and $L = 0$ ground state, respectively.

Field-Dependent Magnetic Torque

Cantilever torque magnetometry is a powerful technique for investigating the magnetic anisotropy of lanthanide-based molecular complexes.[41,42] In this method, a single crystal is mounted on a flexible cantilever and subjected to a static magnetic field. When the crystal is rotated with respect to the field a mechanical torque is exerted on the cantilever, detected via capacitance[43] or piezoresistive[44] readout. The torque originates from the angular dependence of the magnetic free energy imposed by the crystal field Hamiltonian and can be expressed as

$$\tau = \vec{M} \times \vec{B} \quad (13)$$

View Article Online
DOI: 10.1039/D6CP00980H

The amplitude, angular dependence and field evolution of the torque signal therefore provide direct information on both the strength and symmetry of the magnetic anisotropy.[45] In addition, torque measurements allow the orientation of the principal magnetic axes to be determined, an aspect that is often difficult to extract from conventional magnetometry alone. [46,47]

Because the magnetic torque vanishes in isotropic systems, torque magnetometry is intrinsically a single-crystal technique. In a powder sample, the statistical distribution of crystallite orientations causes cancellation of the net torque signal. Despite this requirement, the technique remains experimentally convenient because it can be applied to small crystals over a wide temperature range (typically 2-300K) and its sensitivity to anisotropy is suitable also for poorly anisotropic samples.[48]

In the present work we focus on the low-temperature (2 K) regime and magnetic fields between 1 and 9 T. Under these conditions, the Zeeman interaction dominates and the torque signal reflects the ground state anisotropy. The maximum torque amplitude therefore provides a direct fingerprint of the ground state composition, complementing the saturation magnetization and χT values discussed above.

The simulated torque curves are reported in Figures S8-S18. Their phase is consistent with easy-axis magnetic anisotropy, and the angles at which the torque vanishes correspond to configurations where the easy magnetization direction is either parallel or perpendicular to the applied field.

The maximum torque amplitudes as a function of applied magnetic field are summarized in Table 1 for all lanthanide ions considered. Across the series the torque increases monotonically with field. Particularly large torque values are predicted for Dy^{3+}, Ho^{3+} and Er^{3+}, reflecting their large $|m_J|$ ground states and favourable (i.e. > 1) g_J factors. By contrast, Sm^{3+} displays significantly smaller torque values throughout the entire field range, consistent with its comparatively small g_J.

Table 1 – Maximum magnetic torque as a function of applied field for all trivalent lanthanide ions in the easy axis CF limit ($B_2^0 < 0$), simulated at T = 2 K. Values are reported in N m mol^{-1}. Eu^{3+} and Gd^{3+} have not been included due to their J = 0 and L = 0 ground state, respectively.

	$\tau_{max}(N\,m\,mol^{-1})$										
	Ce^{3+}	Pr^{3+}	Nd^{3+}	Pm^{3+}	Sm^{3+}	Tb^{3+}	Dy^{3+}	Ho^{3+}	Er^{3+}	Tm^{3+}	Yb^{3+}
$B = 1T$	3.97	8.18	8.51	4.89	0.47	39.43	45.22	45.22	39.44	28.05	11.93
$B = 2T$	13.35	24.68	25.49	15.99	1.84	91.33	102.80	102.81	91.37	68.27	33.69
$B = 3T$	24.81	42.88	44.14	29.16	3.97	142.72	159.85	159.87	142.78	108.53	55.68
$B = 4T$	36.93	61.33	63.03	42.88	6.70	193.71	216.49	216.52	193.79	148.34	79.72
$B = 5T$	49.22	79.75	81.83	56.69	9.87	244.39	272.88	272.91	244.50	187.97	102.64
$B = 6T$	61.58	98.08	100.59	70.53	13.35	295.16	328.81	328.84	295.31	227.61	125.47
$B = 7T$	73.91	116.40	119.30	84.33	17.04	345.66	385.20	385.25	345.83	267.11	148.11

$B = 8T$	86.19	134.67	138.01	98.08	20.86	361.49	440.86	440.93	396.38	306.30	170.89
$B = 9T$	98.41	152.76	156.57	118.66	24.81	446.11	497.02	497.09	446.40	345.66	193.42

View Article Online
DOI: 10.1039/D6CP00980H

Angular-Dependent XMCD

X-ray Magnetic Circular Dichroism (XMCD) is a synchrotron-based technique that provides element-specific information on the magnetic properties of a material by measuring the difference in absorption between left- and right- circularly polarized X-rays.[5] The XMCD intensity is proportional to the magnetization projected onto the X-ray propagation vector, which introduces a strong dependence on the relative orientation between the sample's magnetic axes and the incident beam direction.[49] As a results, XMCD provides a direct and sensitive spectroscopic probe of magnetic anisotropy.[50,51]

The high brilliance and energy tunability of synchrotron radiation enable XMCD measurements on extremely small amounts of material[52], making the technique particularly suitable for studying molecular magnetic systems deposited on surfaces, down to the monolayer regime[53–55]. In this work XMCD spectra were simulated for all trivalent lanthanide ions at the $M_{4,5}$ edges, corresponding to the $3d^{10}4f^n \rightarrow 3d^9 4f^{n+1}$ electronic transitions. These edges are accessed using soft X-rays (≈800-1500 eV) and directly probe the 4f shell responsible for the magnetic properties of lanthanide ions.[56] Because the absolute magnitude of the XMCD signal strongly depends on beamline-specific experimental factors, the simulated spectra have been normalized with respect to the isotropic absorption spectrum. Details of the normalization procedure is provided in Supplementary Note S1.

XMCD spectra were simulated at 2 K under magnetic fields ranging from 0 to 6 T, considering field orientations spanning from the principal magnetic z axis ($\theta = 0°$) to the transverse x axis ($\theta = 90°$). The complete angular dependence of the XMCD signal at 6 T, together with the field dependence of the dichroic intensities at both the M_4 and M_5 edges, are reported in Figures S19-S29. Maximum XMCD values at both edges for all ions and field conditions are summarized in Tables S2-S12.

Across the lanthanide series, early ions display a larger dichroic signal at the M_4 edge, whereas from Tb^{3+} onwards the dominant contribution shifts to the M_5 edge. Notably, Yb^{3+} exhibits no signal at the M_4 edge, consistent with its nearly filled $4f^{13}$ configuration, which suppresses the dipole allowed $3d_{3/2} \rightarrow 4f$ transition responsible for the M_4 XMCD signal.[57]

Consistent with easy-axis magnetic anisotropy, the dichroic signal reaches its maximum when the magnetic field is aligned with the z axis ($\theta = 0°$). In this configuration the XMCD intensity rapidly approaches saturation with increasing field, reflecting the stabilization of the highest $|m_J|$ component as ground state. The maximum values obtained at the M_5 edge with $\theta = 0°$ at selected magnetic fields are listed in Table 2. A notable feature is the sign

View Article Online
DOI: 10.1039/D6CP00980H

change of the XMCD signal between early and late lanthanide series, from positive values for Ce^{3+}-Sm^{3+} to negative value from Tb^{3+} onwards, reflecting the reversal of the spin-orbit coupling interaction sign.

When the field is applied within the equatorial plane ($\theta = 90°$), the XMCD signal is strongly reduced and increases approximately linearly with field. This behaviour mirrors the transverse magnetization response discussed above and arises from the same physical mechanism. The angular dependence of the XMCD intensity therefore constitutes a spectroscopic analogue of directional magnetization measurements and provides a direct fingerprint of the 4f ground state anisotropy.

Table 2 – Maximum normalized XMCD signal at the M_5 edge as a function of applied field for all trivalent lanthanide ions in the easy axis crystal field limit ($B_2^0 < 0$), simulated at T = 2 K and X-ray incidence angle $\theta = 0°$. Eu^{3+} and Gd^{3+} have not been included due to their J = 0 and L = 0 ground state, respectively.

	$XMCD_{max}$(%)										
	Ce^{3+}	Pr^{3+}	Nd^{3+}	Pm^{3+}	Sm^{3+}	Tb^{3+}	Dy^{3+}	Ho^{3+}	Er^{3+}	Tm^{3+}	Yb^{3+}
$B = 0.2T$	8.06	16.81	6.79	6.54	2.77	-98.90	-111.89	-115.56	-107.52	-87.58	-52.48
$B = 0.6T$	22.97	45.16	18.19	18.44	8.35	-173.98	-185.27	-191.15	-189.17	-177.45	-133.48
$B = 0.8T$	29.37	55.36	22.25	23.40	10.96	-180.76	-188.61	-196.38	-196.46	-190.88	-158.25
$B = 1.0T$	34.90	62.95	25.25	27.56	13.64	-182.84	-191.71	-197.78	-198.70	-196.39	-174.50
$B = 1.5T$	45.00	73.54	29.38	34.80	20.23	-183.74	-192.20	-198.29	-199.66	-200.00	-193.02
$B = 3.0T$	55.54	79.46	31.65	41.44	38.08	-183.74	-192.20	-198.29	-199.66	-200.00	-200.00

Conclusions

In this work we have established a coherent and quantitative set of benchmark magnetic observables for trivalent lanthanide ions in the ideal easy-axis crystal-field limit. By restricting the description to the ground Jmultiplet and employing a minimal crystal-field model retaining only the axial B_2^0 Stevens' parameter, we generated reference values for the saturation magnetization, low-temperature χT, magnetic torque, and XMCD response across the lanthanide series. To our knowledge, no unified set of reference values encompassing these complementary experimental techniques has previously been reported for lanthanide-based systems.

A practically relevant observation also emerges from this systematic analysis. The "thirds" approximation for powder magnetization averaging introduces systematic deviations in the low-temperature, high-field regime, a non-negligible error for strongly anisotropic systems. These results highlight the importance of performing rigorous spherical averaging when quantitative agreement between simulations and experiments is required.

The reference values presented here are ready-to-use. All simulations were performed under experimentally accessible conditions (T = 2 K, B = 7 T for magnetization, B = 0.1 T for χT; B = 1–9 T for torque; and B = 0–6 T for XMCD) and are intended to facilitate immediate comparison with experimental measurements. Beyond providing a practical framework for

interpreting magnetic data, these benchmarks offer simple yet quantitative guidelines for evaluating if the target easy axis anisotropy of a lanthanide complexes has been experimentally achieved, and for guiding the design of functional molecular magnetic materials.

References

1 M. E. McHenry and D. E. Laughlin, in *Characterization of Materials*, Wiley, 2012, pp. 1–25.

2 E. Moreno-Pineda and W. Wernsdorfer, *Nat. Rev. Phys.*, 2021, **3**, 645–659.

3 P. Lin, T. J. Burchell, L. Ungur, L. F. Chibotaru, W. Wernsdorfer and M. Murugesu, *Angew. Chem. Int. Ed.*, 2009, **48**, 9489–9492.

4 N. A. Bonde, J. B. Petersen, M. A. Sørensen, U. G. Nielsen, B. Fåk, S. Rols, J. Ollivier, H. Weihe, J. Bendix and M. Perfetti, *Inorg. Chem.*, 2020, **59**, 235–243.

5 C. A. F. Vaz, G. van der Laan, S. A. Cavill, H. A. Dürr, A. Fraile Rodríguez, F. Kronast, W. Kuch, P. Sainctavit, G. Schütz, H. Wende, E. Weschke and F. Wilhelm, *Nat. Rev. Methods Prim.*, 2025, **5**, 27.

6 R. Sessoli, M. Mannini, F. Pineider, A. Cornia and P. Sainctavit, in *Magnetism and Synchrotron Radiation*, eds. E. Beaurepaire, H. Bulou, F. Scheurer and J.-P. Kappler, Springer Berlin, Heidelberg, Heidelberg, 2010, pp. 279–311.

7 G. van der Laan, *J. Phys. Conf. Ser.*, 2013, **430**, 012127.

8 A. Raza and M. Perfetti, *Coord. Chem. Rev.*, 2023, **490**, 215213.

9 J. Emerson-King, G. K. Gransbury, B. E. Atkinson, W. J. A. Blackmore, G. F. S. Whitehead, N. F. Chilton and D. P. Mills, *Nature*, 2025, **643**, 125–129.

10 F.-S. Guo, B. M. Day, Y.-C. Chen, M.-L. Tong, A. Mansikkamäki and R. A. Layfield, *Science*, 2018, **362**, 1400–1403.

11 A. H. Vincent, Y. L. Whyatt, N. F. Chilton and J. R. Long, *J. Am. Chem. Soc.*, 2023, **145**, 1572–1579.

12 F. S. Santana, M. Perfetti, M. Briganti, F. Sacco, G. Poneti, E. Ravera, J. F. Soares and R. Sessoli, *Chem. Sci.*, 2022, **13**, 5860–5871.

13 M. Allegrozzi, I. Bertini, M. B. L. Janik, Y.-M. Lee, G. Liu and C. Luchinat, *J. Am. Chem. Soc.*, 2000, **122**, 4154–4161.

14 G. Lorusso, M. Jenkins, P. González-Monje, A. Arauzo, J. Sesé, D. Ruiz-Molina, O. Roubeau and M. Evangelisti, *Adv. Mater.*, 2013, **25**, 2984–2988.

15 P. Konieczny, D. Czernia and T. Kajiwara, *Sci. Rep.*, 2022, **12**, 16601.

16 S. Stoll and A. Schweiger, *J. Magn. Reson.*, 2006, **178**, 42–55.

View Article Online
DOI: 10.1039/D6CP00980H

17 M. W. Haverkort, *J. Phys. Conf. Ser.*, 2016, **712**, 012001.

18 J. Luzon and R. Sessoli, *Dalt. Trans.*, 2012, **41**, 13556.

19 J. Tang and P. Zhang, *Lanthanide Single Molecule Magnets*, Springer Berlin Heidelberg, Berlin, Heidelberg, 2015.

20 L. Sorace and D. Gatteschi, in *Lanthanides and Actinides in Molecular Magnetism*, eds. R. A. Layfield and M. Murugesu, Wiley, 2015, pp. 1–26.

21 A. S. Manvell, R. Pfleger, N. A. Bonde, M. Briganti, C. A. Mattei, T. B. Nannestad, H. Weihe, A. K. Powell, J. Ollivier, J. Bendix and M. Perfetti, *Chem. Sci.*, 2024, **15**, 113–123.

22 J. Sievers, *Zeitschrift fur Phys. B Condens. Matter*, 1982, **45**, 289–296.

23 J. D. Rinehart and J. R. Long, *Chem. Sci.*, 2011, **2**, 2078–2085.

24 M. Briganti, E. Lucaccini, L. Chelazzi, S. Ciattini, L. Sorace, R. Sessoli, F. Totti and M. Perfetti, *J. Am. Chem. Soc.*, 2021, **143**, 8108–8115.

25 C. Rudowicz and C. Y. Chung, *J. Phys. Condens. Matter*, 2004, **16**, 5825–5847.

26 M. Atzori, E. Morra, L. Tesi, A. Albino, M. Chiesa, L. Sorace and R. Sessoli, *J. Am. Chem. Soc.*, 2016, **138**, 11234–11244.

27 M. Perfetti, M. Gysler, Y. Rechkemmer-Patalen, P. Zhang, H. Taştan, F. Fischer, J. Netz, W. Frey, L. W. Zimmermann, T. Schleid, M. Hakl, M. Orlita, L. Ungur, L. Chibotaru, T. Brock-Nannestad, S. Piligkos and J. van Slageren, *Chem. Sci.*, 2019, **10**, 2101–2110.

28 P. Kumar, S. Biswas, A. Swain, J. Acharya, V. Kumar, P. Kalita, J. F. Gonzalez, O. Cador, F. Pointillart, G. Rajaraman and V. Chandrasekhar, *Inorg. Chem.*, 2021, **60**, 8530–8545.

29 P. Evans, D. Reta, G. F. S. Whitehead, N. F. Chilton and D. P. Mills, *J. Am. Chem. Soc.*, 2019, **141**, 19935–19940.

30 P. Kumar, A. Swain, J. Acharya, Y. Li, V. Kumar, G. Rajaraman, E. Colacio and V. Chandrasekhar, *Inorg. Chem.*, 2022, **61**, 11600–11621.

31 J. Emerson-King, J. Baldwin, S. C. Corner, W. J. A. Blackmore, N. F. Chilton and D. P. Mills, *J. Am. Chem. Soc.*, 2025, **147**, 35555–35566.

32 A. Konstantatos, M. A. Sørensen, J. Bendix and H. Weihe, *Dalt. Trans.*, 2017, **46**, 6024–6030.

33 F. Pointillart, B. le Guennic, O. Cador, O. Maury and L. Ouahab, *Acc. Chem. Res.*, 2015, **48**, 2834–2842.

34 U. Köbler and A. Hoser, *J. Magn. Magn. Mater.*, 2014, **349**, 88–94.

View Article Online
DOI: 10.1039/D6CP00980H

35 V. I. Lebedev, *USSR Comput. Math. Math. Phys.*, 1976, **16**, 10–24.

36 M. Edén and M. H. Levitt, *J. Magn. Reson.*, 1998, **132**, 220–239.

37 M. Edén, *Concepts Magn. Reson. Part A*, 2003, **18A**, 24–55.

38 R. Boča, *Theoretical foundations of molecular magnetism*, Elsevier, Amsterdam, 1999, vol. 1.

39 H. Schilder and H. Lueken, *J. Magn. Magn. Mater.*, 2004, **281**, 17–26.

40 O. Kahn, *Molecular Magnetism*, VCH Publishers, New York, 1993.

41 L. Tacconi, A. Cini, A. Raza, L. Tesi, P. Bartolini, A. Taschin, J. van Slageren, M. Briganti, L. Sorace, M. Fittipaldi and M. Perfetti, *J. Am. Chem. Soc.*, 2025, **147**, 33040–33051.

42 M. Perfetti, E. Lucaccini, L. Sorace, J. P. Costes and R. Sessoli, *Inorg. Chem.*, 2015, **54**, 3090–3092.

43 C. Rossel, M. Willemin, A. Gasser, H. Bothuizen, G. I. Meijer and H. Keller, *Rev. Sci. Instrum.*, 1998, **69**, 3199–3203.

44 M. Willemin, C. Rossel, J. Brugger, M. H. Despont, H. Rothuizen, P. Vettiger, J. Hofer and H. Keller, *J. Appl. Phys.*, 1998, **83**, 1163–1170.

45 L. Tacconi, A. S. Manvell, M. Briganti, D. Czernia, H. Weihe, P. Konieczny, J. Bendix and M. Perfetti, *Angew. Chem. Int. Ed.*, 2025, **137**, e202417582.

46 L. Tacconi, V. Adebayo, L. Chelazzi, C. Berthon, H. Bolvin and M. Perfetti, *J. Am. Chem. Soc.*, 2026, **148**, 1106–1115.

47 L. Rigamonti, A. Cornia, A. Nava, M. Perfetti, M.-E. Boulon, A.-L. Barra, X. Zhong, K. Park and R. Sessoli, *Phys. Chem. Chem. Phys.*, 2014, **16**, 17220.

48 J. T. Janetzki, A. Raza, M. Briganti, R. Duquennoy, A.-L. Barra, C. Toninelli, M. Perfetti and L. Sorace, *J. Am. Chem. Soc.*, 2026, **148**, 11260–11273.

49 B. T. Thole, P. Carra, F. Sette and G. Van Der Laan, *Phys. Rev. Lett.*, 1992, **68**, 1943.

50 L. Tacconi, S. S. Leiszner, M. Briganti, G. Cucinotta, E. Otero, M. Mannini and M. Perfetti, *Small*, 2024, **20**, 2401627.

51 S. O. Parreiras, D. Moreno, B. Cirera, M. A. Valbuena, J. I. Urgel, M. Paradinas, M. Panighel, F. Ajejas, M. A. Niño, J. M. Gallego, M. Valvidares, P. Gargiani, W. Kuch, J. I. Martínez, A. Mugarza, J. Camarero, R. Miranda, P. Perna and D. Écija, *Small*, 2021, **17**, 2102753.

52 E. Beaurepaire, H. Bulou, L. Joly and F. Scheurer, Eds., *Magnetism and Synchrotron Radiation: Towards the Fourth Generation Light Sources*, Springer International Publishing, Cham, 2013, vol. 151.

View Article Online
DOI: 10.1039/D6CP00980H

53 J. Dreiser, *J. Phys. Condens. Matter*, 2015, **27**, 183203.

54 M. Mannini, F. Bertani, C. Tudisco, L. Malavolti, L. Poggini, K. Misztal, D. Menozzi, A. Motta, E. Otero, P. Ohresser, P. Sainctavit, G. G. Condorelli, E. Dalcanale and R. Sessoli, *Nat. Commun.*, 2014, **5**, 4582.

55 G. Serrano, E. Velez-Fort, I. Cimatti, B. Cortigiani, L. Malavolti, D. Betto, A. Ouerghi, N. B. Brookes, M. Mannini and R. Sessoli, *Nanoscale*, 2018, **10**, 2715–2720.

56 S. Tripathi, Max-Planck-Institut für Intelligente Systeme, 2018.

57 V. N. Antonov and D. A. Kukusta, *Phys. Rev. B*, 2019, **99**, 104403.

The authors confirm that the data supporting the findings of this study are available within the article and its supplementary materials.

View Article Online
DOI: 10.1039/D6CP00980H